PHYSICAL REVIEW B **92**, 024109 (2015)

Structural and magnetic phase transitions in $EuTi_{1-x}Nb_xO_3$

Ling Li,[1] James R. Morris,[1,2] Michael R. Koehler,[1] Zhiling Dun,[3] Haidong Zhou,[3] Jiaqiang Yan,[1,2] David Mandrus,[1,2] and Veerle Keppens[1]

[1]*Department of Materials Science and Engineering, University of Tennessee, Knoxville, Tennessee 37996, USA*
[2]*Materials Science and Technology Division, Oak Ridge National Laboratory, Oak Ridge, Tennessee 37831, USA*
[3]*Department of Physics and Astronomy, University of Tennessee, Knoxville, Tennessee 37996, USA*

(Received 20 May 2015; published 30 July 2015)

We have investigated the structural and magnetic phase transitions in $EuTi_{1-x}Nb_xO_3$ ($0 \leqslant x \leqslant 0.3$) with synchrotron powder x-ray diffraction, resonant ultrasound spectroscopy, and magnetization measurements. Upon Nb doping, the $Pm\bar{3}m \leftrightarrow I4/mcm$ structural transition shifts to higher temperatures and the room temperature lattice parameter increases while the magnitude of the octahedral tilting decreases. In addition, Nb substitution for Ti destabilizes the antiferromagnetic ground state of the parent compound and long-range ferromagnetic order is observed in the samples with $x \geqslant 0.1$. The structural transition in pure and doped compounds is marked by a dramatic steplike softening of the elastic moduli near T_S, which resembles that of $SrTiO_3$ and can be adequately modeled using the Landau free energy model employing the same coupling between strain and octahedral tilting order parameter as previously used to model $SrTiO_3$.

DOI: 10.1103/PhysRevB.92.024109 PACS number(s): 75.85.+t, 64.70.Nd, 81.30.Bx

I. INTRODUCTION

The tilting of the oxygen octahedra in cubic perovskites is known to induce structural phase transitions, which are often associated with the emergence of intriguing physical phenomena [1]. $SrTiO_3$ (STO) is one of the most extensively studied perovskite oxides for its structural phase transition (SPT) at $T_S \approx 105$ K [2,3]. This SPT has been recognized as the paradigm of a displacive transition, nevertheless, proven to carry some order/disorder element [4,5]. In the past decade, the discovery of the magnetoelectric coupling in isostructural $EuTiO_3$ (ETO) has generated substantial interest in this compound [6]. This coupling manifests itself in a significant decrease of the dielectric constant at the *G*-type antiferromagnetic ordering temperature $T_N \approx 5.6$ K [6]. In analogy to STO, ETO also undergoes an antiferrodistortive SPT from $Pm\bar{3}m$ to $I4/mcm$ ($a^0a^0c^-$ in Glazer notation) driven by *R*-point phonon softening [7]. While the SPT at 105 K in STO has been extensively studied for decades, the transition in ETO was observed only recently [8] but has since attracted much attention in the field and has been the focus of numerous experimental [7,9–15] and theoretical [16–18] studies.

Previous synchrotron powder x-ray diffraction (XRD) indicates a $T_S \approx 235$ K for ETO [10], which is significantly lower than $T_A \approx 282$ K suggested by heat capacity measurement [8]. This discrepancy draws attention to the possible local tetragonal distortions present above 235 K, as evidenced by pair distribution function analysis [10]. Kim *et al.* [13] identified incommensurate satellite peaks below 285 K in single-crystal synchrotron XRD, and proposed a dynamically modulated equilibrium state between 285 K and 160 K, incorporating antiferrodistortive instabilities of TiO_6 octahedra accompanied by antiferroelectric displacements of Ti atoms. Conversely, a simple and unmodulated structure is claimed for ETO, as evidenced by the commensurate superlattice peaks at $T = 250$ K in single-crystal XRD [14], and the *R*-point acoustic phonon softening that is similar to the soft modes in STO [7]. ETO samples synthesized under different conditions were studied [11]. While one of the ceramic samples shows a simple cubic-to-tetragonal long-range transformation near 300 K, the other ceramic samples as well as the single crystal present an incommensurate structure at low temperature. These discrepancies were considered to arise from variations in sample preparation conditions, which lead to mixed valence on the Eu site and/or oxygen nonstoichiometry and therefore could potentially alter the physical properties. This was further confirmed by Kennedy *et al.* [19], who show that the electrical resistivity of $EuTiO_{3-\delta}$ is significantly reduced with oxygen vacancies due to the change of Ti^{4+} to Ti^{3+} when oxygen vacancies and/or trivalent Eu are present. Very recently, the elastic response near 1 MHz of an irregularly shaped ETO single crystal was examined using resonant ultrasound spectroscopy (RUS) [20]. A pronounced steplike shear softening near $T_S \approx 284$ K confirms that the SPT in STO and ETO is very similar in nature but takes place at very different temperatures.

Despite the recent studies of the nature and T_S of the SPT in ETO, the dramatic difference in T_S between STO and ETO is not well understood (the Goldschmidt tolerance factor *t* predicts a similar T_S for these two compounds) and may signal the importance of the spin-phonon coupling in ETO [21]. First-principles calculations suggested that the hybridization between Eu-*f* and Ti-*d* orbitals enhances the tilting of the octahedra and therefore T_S [18]. To examine how the T_S of the ETO system is influenced by the hybridization between Eu-*f*, (Ti, Nb)-*d*, and O-*p* orbitals, we have initiated the study of $EuTi_{1-x}Nb_xO_3$. Nb doping introduces itinerant electrons into this system, which mediate the magnetic interactions between Eu $4f$ spins and result in ferromagnetism [22]. In the present paper, we extend the RUS study by Spalek *et al.* [20] and report the full elastic tensor of single crystals of ETO as well as mixed crystals of $EuTi_{1-x}Nb_xO_3$. The dramatic change in the elastic constants allows for an accurate determination of T_S, and the potential impact of the orbital hybridization on T_S can be addressed. The amplitude of octahedral rotations at 100 K is determined from synchrotron x-ray powder diffraction data, and the role of Nb doping on the structural and magnetic instabilities will be discussed.

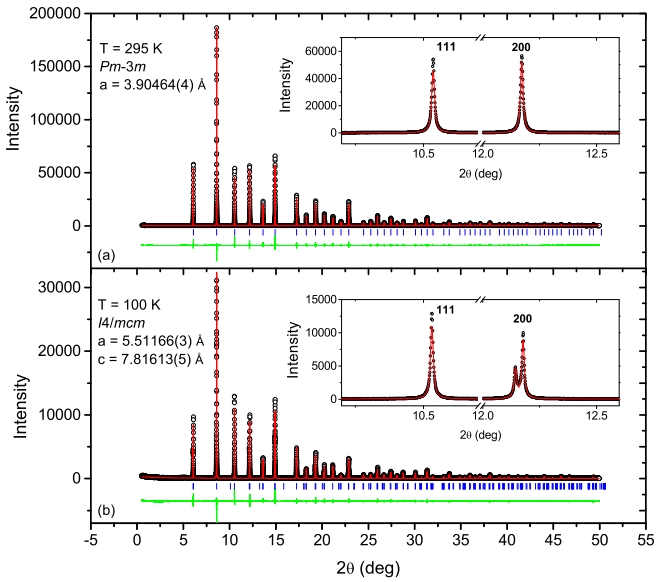

FIG. 1. (Color online) Rietveld refinements of the synchrotron x-ray powder patterns of $EuTiO_3$ collected at (a) 295 K and (b) 100 K. The insets show the (111) and (200) reflections.

II. METHODS

$EuTi_{1-x}Nb_xO_3$ polycrystals ($0 \leqslant x \leqslant 0.3$) and single crystals ($x = 0$, 0.05, 0.1, and 0.2) have been synthesized. The polycrystalline samples were prepared using a conventional solid-state reaction method as described in Ref. [22]. The single-crystal growth was carried out in a double-ellipsoidal-mirror image furnace (NEC) in 90:10 Ar:H_2 atmosphere. The pulling speed was 10 mm/h with feed and seed rods rotating in opposite directions at 25 rpm. Good crystal quality was confirmed by clear, round spots in the Laue back-scattering pattern. The single crystals were oriented with $Pm\bar{3}m$ symmetry using the software OrientExpress and cut into rectangular parallelepipeds with all faces perpendicular to the crystallographic ⟨100⟩ axes for RUS measurements. The edge dimensions of the $EuTi_{1-x}Nb_xO_3$ ($x = 0$, 0.05, 0.1) single crystals for RUS measurements range between 0.5 mm and 2.5 mm. RUS is a technique developed by Migliori *et al.* [23] for determining the complete elastic tensor of a small single crystal by measuring its free-body resonances. It allows determination of the full elastic tensor without needing to change transducers or remounting the sample.

Room and low temperature x-ray diffraction (XRD) was first performed with a laboratory Huber imaging plate Guinier camera 670 with Ge monochromatized $CuK_{\alpha 1}$ radiation ($\lambda = 1.54059$ Å), confirming all samples to be single phase. To better resolve the tetragonal distortion, synchrotron powder XRD was performed through a mail-in program at the 11-BM beamline of the Advanced Photon Source at Argonne National Laboratory. Single crystals of $EuTi_{1-x}Nb_xO_3$ ($x = 0$, 0.05, 0.1, and 0.2) were ground to fine powders and loaded in a capillary tube with a diameter of 0.8 mm. The experiments were carried out with a fixed wavelength [$E = 30$ keV, $\lambda = 0.41396(1)$ Å] at $T = 295$ K and 100 K. Rietveld refinements were obtained using the program GSAS [24].

The magnetization measurements were performed using a Quantum Design magnetic property measurement system in the temperature interval 2 K to 300 K after cooling in either zero field (ZFC) or in a measuring field (FC). Thermogravimetric analysis (TGA) was employed to determine the oxygen content of ETO from the weight gain due to oxidation of Eu^{2+} to Eu^{3+}. The ETO crystals were found to be oxygen stoichiometric within experimental error.

III. RESULTS

A. X-ray diffraction

Figures 1(a) and 1(b) show the Rietveld refinements from synchrotron XRD for the parent ETO at 295 K and 100 K, respectively. While the pattern at 295 K was refined with the $Pm\bar{3}m$ space group with lattice parameter $a = 3.9047(3)$ Å, the pattern at 100 K was refined using $I4/mcm$ symmetry, yielding lattice parameters $a_{\text{Tetra}} = \sqrt{2}a_{\text{Cub}} = 5.51168(3)$ Å and $c_{\text{Tetra}} = 2c_{\text{Cub}} = 7.81613(5)$ Å, in good agreement with previously reported values [10]. Furthermore, the 295 K synchrotron XRD patterns of all samples show no well-defined peak splitting and could be adequately fitted with a cubic $Pm\bar{3}m$ model, whereas the 100 K patterns show well-resolved peak splitting and were fitted with a tetragonal $I4/mcm$ model. The room temperature lattice parameter extracted from Rietveld refinements obeys Vegard's law, and increases

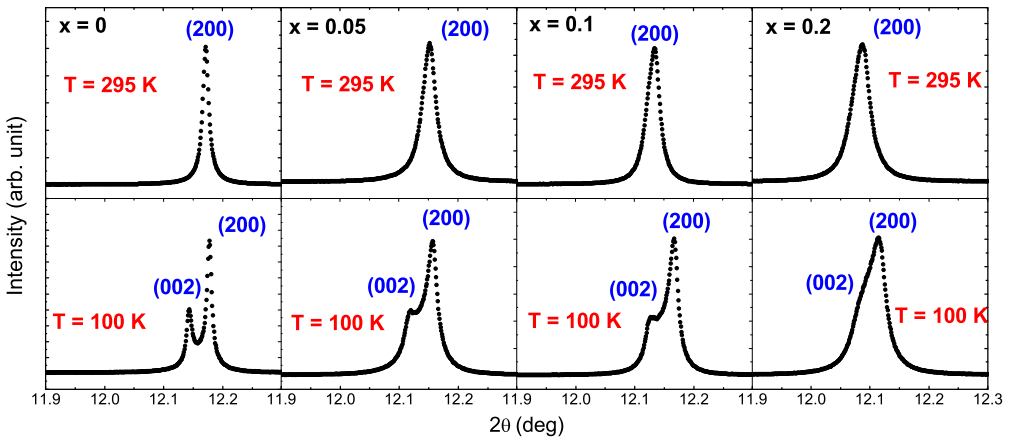

FIG. 2. (Color online) (200) reflection at 295 K (top) and 100 K (bottom) for $EuTi_{1-x}Nb_xO_3$ ($x = 0$, 0.05, 0.1, and 0.2).

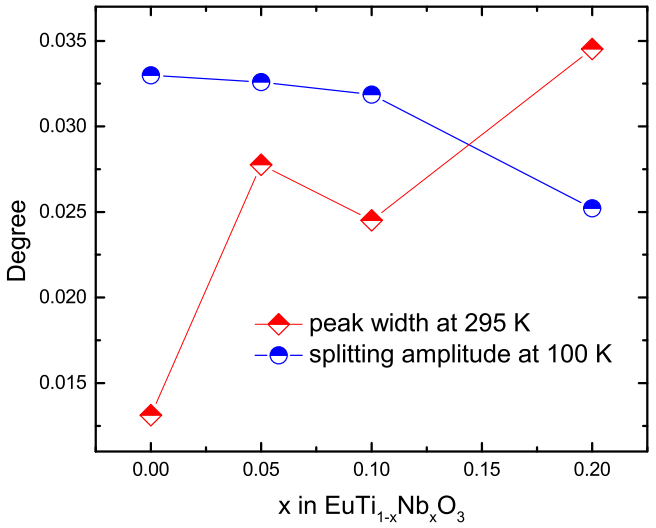

FIG. 3. (Color online) The (200) peak width at 295 K and splitting amplitude at 100 K for $EuTi_{1-x}Nb_xO_3$ ($x = 0$, 0.05, 0.1, 0.2).

linearly with increasing x in $EuTi_{1-x}Nb_xO_3$. The symmetry lowering at 100 K was evidenced by the (200) peak splitting highlighted in the insets to Fig. 1.

As shown in Fig. 2, no readily apparent peak splitting due to the structural transition was observed at room temperature. However, we noticed significant peak broadening with increasing Nb content. This is demonstrated more clearly in Fig. 3 in which we plotted the peak width of the (200) reflection at 295 K and splitting amplitude of (200) at 100 K obtained by a Lorentzian fit. Nb doping induces disorder in the lattice, which can naturally explain the peak broadening. However, we believe that the peak splitting due to the structural transition also contributes to the peak broadening at 295 K since the SPT takes place above room temperature as revealed by RUS measurements. Intriguingly, the splitting amplitude at 100 K, which is proportional to the magnitude of the lattice distortion c/a ratio, is suppressed with increasing Nb doping, suggesting that Nb doping weakens the octahedral tilting in the ETO system.

B. Magnetization

Figure 4 shows the temperature dependence of magnetization for $EuTi_{1-x}Nb_xO_3$ single crystals, plotted as (a) M/H under 50 Oe, and (b) H/M under 1000 Oe. The ZFC and FC curves of the parent ETO overlap and reveal a $T_N \approx 5.7$ K. The data under 1000 Oe between 200 K and 300 K could be well fitted by the Curie-Weiss law, yielding a positive Weiss temperature of 3.48(1) K and an effective moment of approximately 8.35(1) μ_B, which agree well with literature values [6]. A dramatic divergence between ZFC and FC curves is present for the $x = 0.05$ sample, which may signal a spin glass behavior arising from the competition between AFM and FM interactions present in this system. The magnetic ground state of samples with $x \geqslant 0.1$ is switched from AFM to FM, as previously reported for polycrystalline samples [22]. It is noteworthy that Nb doping induces metallic behavior [22]. The induced ferromagnetism most likely results from the ferromagnetic interaction between localized Eu $4f$ spins, mediated by itinerant electrons introduced by chemical doping [22,25].

C. Elastic moduli

Cubic systems exhibit three independent elastic constants C_{11}, C_{12}, and C_{44}. Note that C_{11} and C_{44} govern respectively longitudinal and transverse waves propagating along [100]. In the [110] direction, longitudinal waves are governed by $C_{L[110]} = \frac{1}{2}(C_{11} + C_{12} + 2C_{44})$, while one transverse wave is governed by C_{44}, the other by $C_{T[110]} = \frac{1}{2}(C_{11} - C_{12}) = C'$. In Fig. 5 we plot the temperature dependence of C_{44}. Below T_S, the ultrasonic absorption of the sample is so large that not enough resonances can be observed to allow an accurate determination of all three elastic moduli. However,

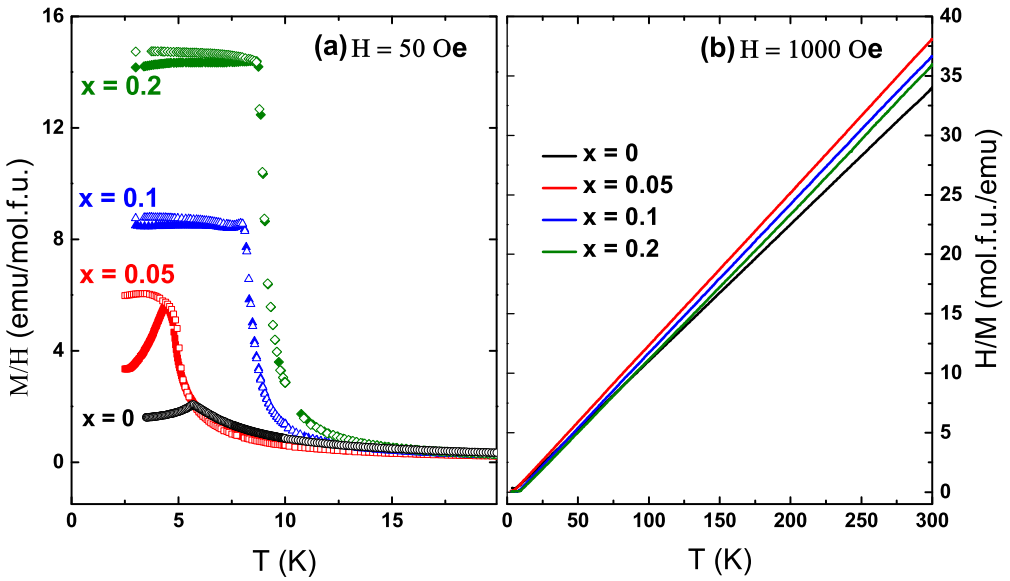

FIG. 4. (Color online) Temperature dependence of magnetization for single crystals of $EuTi_{1-x}Nb_xO_3$ ($x = 0$, 0.05, 0.1, 0.2). Note that the full and empty symbols in (a) denote ZFC and FC data, respectively.

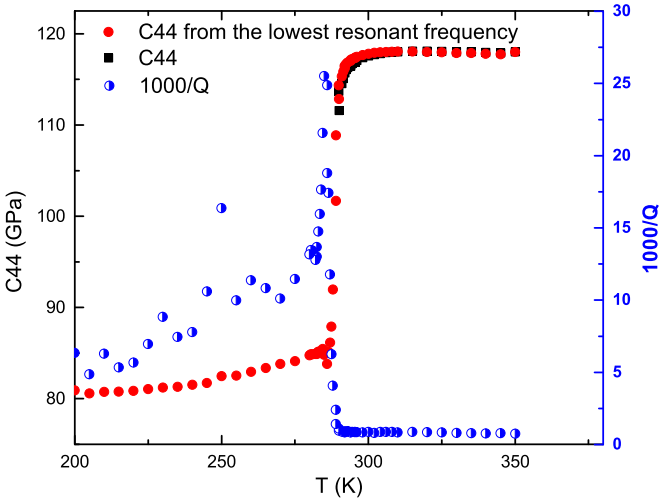

FIG. 5. (Color online) Temperature dependence of the shear modulus C_{44} and the inverse of the quality factor Q, which is defined as the center frequency of the resonance divided by full width at half maximum, of an oriented ETO single crystal. Note that below the structural phase transition temperature, C_{44} is determined directly from the first resonance peak (red circles).

the high-temperature fit indicates that the lowest resonant frequency depends almost exclusively on C_{44}. This frequency is visible throughout the entire transition and below, allowing determination of the shear modulus over the entire temperature range. The striking feature in Fig. 5 is the steplike elastic softening of C_{44} at $T_S \approx 288$ K, which is reminiscent of the 105 K elastic anomaly observed in the elastic moduli of STO [26]. The softening at T_S is accompanied by a dramatic rise in the internal friction Q^{-1} as a consequence of domain wall motion driven by elastic waves, which causes a significant broadening and deterioration of the resonances, preventing determination of the full tensor, as discussed above.

Figure 6 presents the temperature dependence of C_{11}, C_{44}, and C' for single crystals of $EuTi_{1-x}Nb_xO_3$ ($x = 0$, 0.05, and 0.1) both in the absence of field and under applied magnetic fields up to 3 T. The main features are as follows:

(1) The substitution of Nb^{4+} for Ti^{4+} (up to $x = 0.1$) does not change the qualitative behavior of the elastic response near the SPT, and the steplike elastic softening as the temperature approaches T_S remains the most striking feature.

(2) The transition temperature T_S is shifted to higher temperatures with increasing Nb doping, $T_S = 288$ K, 322 K, and 353 K for $x = 0$, 0.05, and 0.1, respectively.

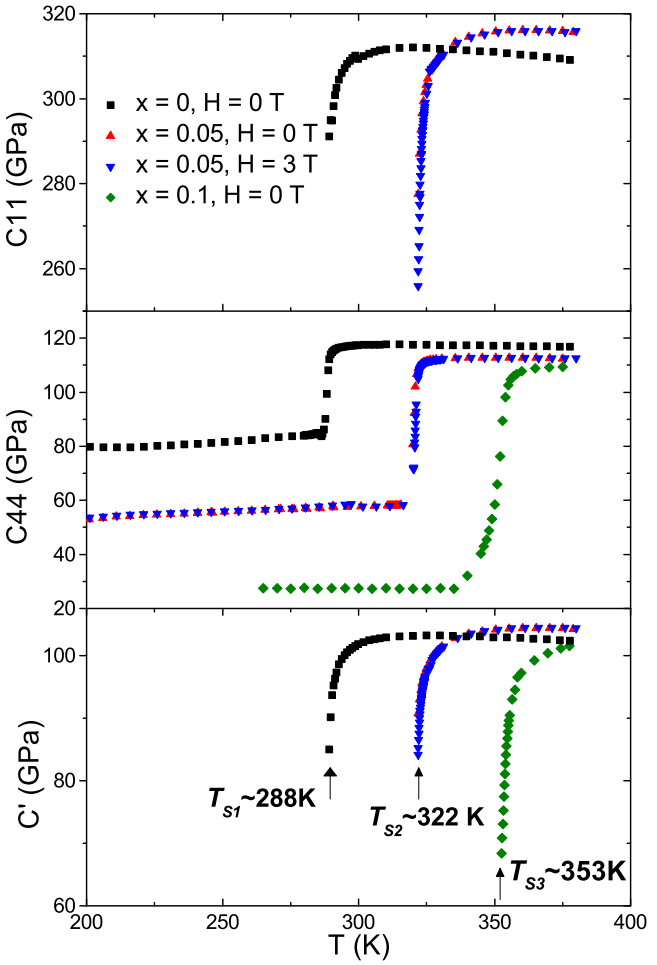

FIG. 6. (Color online) Temperature dependence of elastic constants for single crystals of $EuTi_{1-x}Nb_xO_3$ ($x = 0$, 0.05, and 0.1) in different magnetic fields. Measurements were performed during cooling.

(3) The elastic response of $EuTi_{0.95}Nb_{0.05}O_3$ does not show an observable field dependence up to 3 T.

Table I shows the T_S, density ρ, and the values of the elastic moduli for various samples. The data for single crystals of STO is obtained from the present RUS study. It can be clearly seen that the absolute values of the moduli for STO and ETO are very close.

Figure 7 shows the temperature dependence of C_{44} for polycrystalline samples of $EuTi_{1-x}Nb_xO_3$ ($x = 0$, 0.03, 0.05, 0.1, 0.2, and 0.3). Because the porosity of the ceramic sample

TABLE I. T_S, density, and elastic moduli for single crystals of STO, ETO, and ETO-Nb.

Sample	T_S (K)	Theoretical Density ρ (g/cm^3)	Density ρ (g/cm^3)	C_{11} (GPa)	C_{44} (GPa)	C' (GPa)	Error %
STO	105	5.110	5.015	311.38[a]	120.83[a]	107.20[a]	0.3507
ETO	288	6.914	6.744	307.24[a]	116.30[a]	100.06[a]	0.2323
ETO	288	6.914	6.744	309.76[b]	116.95[b]	102.57[b]	0.2833
ETO-5%Nb	322	6.939	6.809	316.07[b]	112.56[b]	104.37[b]	0.1467
ETO-10 %Nb	353	6.970	6.758	306.29[b]	109.23[b]	100.32[b]	0.3138

[a]Elastic moduli measured at 295 K.
[b]Elastic moduli measured at 370 K.

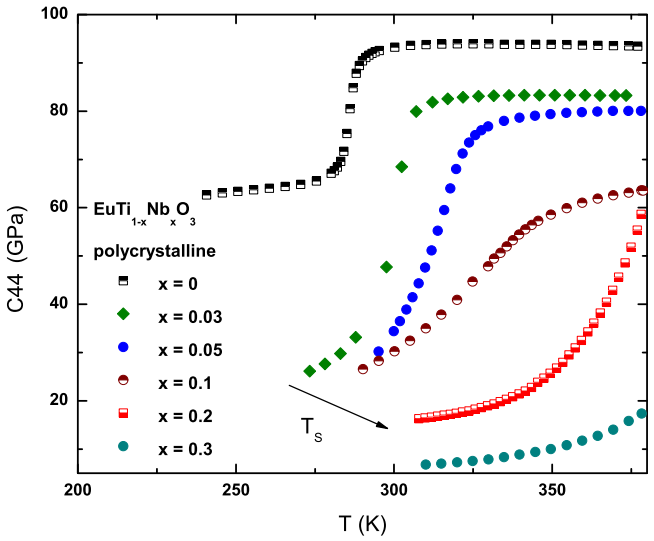

FIG. 7. (Color online) Temperature dependence of the shear modulus C_{44} for polycrystalline $EuTi_{1-x}Nb_xO_3$ ($x = 0$, 0.03, 0.05, 0.1, 0.2, and 0.3). Data are shifted for clarity. Measurements were performed during cooling.

changes the density, and therefore the absolute value of the elastic moduli, we are only interested in the qualitative behavior, and to improve clarity the curves are offset along the y axis. The structural phase transition in $EuTi_{1-x}Nb_xO_3$ is marked by a steplike softening, which is significantly smeared out due to the presence of grains in polycrystalline samples. However, the trend that is clearly observed from Fig. 7 is that T_S increases with increasing Nb concentration and goes beyond our experimental range of 380 K when x reaches 0.2.

IV. DISCUSSION

A. Landau theory

The elastic behavior of a material without any thermodynamic "anomalies" can be modeled using the Varshni function [27]

$$C_{ij}(T) = C_{ij}^0 - \frac{s}{e^{t/T} - 1}, \tag{1}$$

which predicts a gradual stiffening with decreasing temperature that levels off at low temperatures. The elastic behavior of pure ETO obviously deviates from Varshni behavior.

Landau theory is known to provide a proper framework for a formal analysis of phase transitions [28], whereby the free energy can be expressed in terms of strain e_i and order parameter components Q_i. Slonczewski *et al.* [29] performed a Landau analysis of the elastic behavior of $SrTiO_3$ in the 1970s, and here we present calculations using the Landau model for the $EuTiO_3$ system, adapting some of the notations used in [29]. Note that inelastic x-ray scattering has identified zone boundary R-point q =(0.5 0.5 0.5) acoustic phonon softening at this SPT [7]. Thus the amplitudes of the degenerate zone boundary soft acoustic modes Q_1, Q_2, Q_3 can be naturally employed as the order parameter. Considering the crystal symmetry, the free energy F should include an antiferrodistortive energy $F(Q_1, Q_2, Q_3)$, the elastic energy $F(e)$, and a contribution from coupling between the order parameter and strain $F(Q,e)$:

$$F(Q_1, Q_2, Q_3) = A_1\left(Q_1^2+Q_2^2+Q_3^2\right)+A_2\left(Q_1^2 + Q_2^2 + Q_3^2\right)^2 + A_3\left(Q_1^2Q_2^2 + Q_2^2Q_3^2 + Q_3^2Q_1^2\right), \tag{2}$$

$$F(e) = \tfrac{1}{2}C_{11}^c\left(e_1^2 + e_2^2 + e_3^2\right) + C_{12}^c(e_1e_2 + e_2e_3 + e_3e_1) + \tfrac{1}{2}C_{44}^c\left(e_4^2 + e_5^2 + e_6^2\right), \tag{3}$$

$$F(Q,e) = -B_1\left(e_1Q_1^2 + e_2Q_2^2 + e_3Q_3^2\right) - B_2\Big(e_1\left(Q_2^2 + Q_3^2\right) + e_2\left(Q_1^2 + Q_3^2\right) + e_3\left(Q_1^2 + Q_2^2\right)\Big) - B_t(e_4Q_2Q_3 + e_5Q_3Q_1 + e_6Q_1Q_2). \tag{4}$$

Here C_{11}^c, C_{12}^c, and C_{44}^c are elastic moduli in the cubic phase, A_1, A_2, A_3 are Landau expansion coefficients, and B_1, B_2, B_t are coupling constants.

Assuming that the volume strain does not couple to the order parameter, this gives

$$B_e \equiv -B_2 = +\tfrac{1}{2}B_1. \tag{5}$$

Under the equilibrium conditions $\frac{dF}{dQ} = 0, \frac{dF}{de} = 0$ this gives

$$e_i = \frac{B_e\left(3Q_i^2 - Q^2\right)}{C_{11}^c - C_{44}^c}\ \left(i = 1,2,3;\ Q^2 = Q_1^2 + Q_2^2 + Q_3^2\right),$$
$$e_4 = \frac{B_tQ_2Q_3}{C_{44}^c}, \text{etc.} \tag{6}$$

The elastic constants are the second derivatives of the free energy F with respect to strain and may be calculated using the Slonczewski-Thomas formalism [29]

$$C_{ij} = C_{ij}^c - M^{-1}\sum_k \frac{\partial^2 F}{\partial e_i \partial Q_k}\omega_k^{-2}\frac{\partial^2 F}{\partial Q_k \partial e_j}. \tag{7}$$

Substituting (2) $\rightarrow$ (6) into (7) and assuming $Q = (0,0,Q_s)$, we obtain the elastic moduli in the tetragonal phase:

$$C_{11} = C_{11}^c - D, \quad C_{44} = C_{44}^c - E,$$
$$C_{12} = C_{12}^c - D, \quad C_{33} = C_{11}^c - 4D,$$
$$C_{13} = C_{12}^c + 2D, \quad C_{66} = C_{44}^c,$$

where $D = (4B_e^2Q_s^2)/(M\omega_3^2)$, and $E = (B_t^2Q_s^2)/(M\omega_2^2)$. M is the mass density of the oxygen atoms participating in each optical vibration mode, and ω_i ($i = 1,2,3$) are the natural frequencies of these vibration modes. Thus, as the cubic to tetragonal SPT is approached, a steplike softening is expected in the elastic moduli C_{11}, C_{12}, C_{44}, C_{33}, steplike stiffening is expected for C_{13}, and C_{66} is expected to follow the trend of the cubic shear modulus C_{44}. The steplike softening is clearly observed for C_{44} (Fig. 5), and even though the large absorption below T_S prevents us from determining the full elastic tensor below the transition, the precipitous drop in C_{11} and C' (Fig. 6) strongly suggests that these moduli undergo a similar steplike softening. While our Landau analysis predicts such behavior for the longitudinal modulus C_{11}, $C' = \frac{1}{2}(C_{11} - C_{12})$ is expected to smoothly continue through the SPT. This is clearly not observed in C'. Interestingly, the same discrepancy is found in STO [26], and remains unexplained.

B. Precursor effect

In every aspect, the elastic response of ETO through the SPT appears to be very similar to that of STO, which is not surprising in light of the resemblance between their phonon behaviors [3,7]. The SPT in both STO and ETO is driven by a condensation of zone-boundary phonon modes, which is indicative of the displacive nature of both SPTs. From a lattice dynamics point of view, precursor effects have been observed in STO by birefringence measurements [30], where fluctuating ferroelastic clusters form above T_S. Nevertheless, the TA-TO mode coupling which exists in STO and explains its precursor effects is actually absent in ETO [31]. The large neutron absorption inherent to Eu and the difficulty in growing large ETO crystals significantly hamper inelastic neutron experiments and further information regarding the phonon behavior has not yet been obtained. However, our observation of a gentle rounding rather than a sharp step in C_{ij} indicates that the precursor effect takes place in ETO starting about 20 K above T_S, where local elastic nanoregions develop. This is consistent with the pair distribution analysis [10] that showed that the dynamic fluctuations occur above T_S; i.e., tetragonal twinning segments form along three crystallographic orientations. This unexpected precursor effect in ETO has been analyzed by normalizing the transverse modes and taking the derivatives of the modes with respect to momentum, yielding the softening of the transverse acoustic mode as a function of temperature [32]. The coupling between the TA mode and the elastic constants gives rise to the elastic softening as the SPT is approached. Furthermore, the presence of the precursor effect suggests that the transition is not purely of the displacive type, but includes elements of an order/disorder transition.

C. Effect of Nb doping

Figure 8 presents the $EuTi_{1-x}Nb_xO_3$ phase diagram with the structural and magnetic transition temperatures as a function of Nb content (T_N for $x = 0.015$, 0.03, and T_C for $x \geqslant 0.3$ samples are taken from Ref. [22]). The magnetic ground state changes from AFM to FM when $x \geqslant 0.1$. While T_N gradually decreases from 5.7 K ($x = 0$) to 4.5 K ($x = 0.05$), T_C increases slightly from 8.2 K ($x = 0.1$) to a maximum of 9.3 K ($x = 0.2$), and decreases with further Nb doping. Structurally, Nb doping enhances T_C from 288 K ($x = 0$) to 353 K ($x = 0.1$). Nevertheless, the lattice distortion at 100 K is weakened with increasing Nb content. The well-established tolerance factor t concept predicts the symmetry of ABO_3 perovskites structure, with $t = \frac{r_A + r_O}{\sqrt{2}(r_B + r_O)}$, and r_A, r_B, and r_O are the ionic radii of each ion. The radius of Nb^{4+} ($r = 0.68$ Å) is greater than that of Ti^{4+} ($r = 0.605$ Å) [33], which means that substituting Nb for Ti reduces the tolerance factor and promotes the oxygen rotating instabilities. This is in favor of the cubic to tetragonal transformation occurring at higher temperatures with increasing Nb doing, as confirmed by RUS results. Nevertheless, this tolerance factor model, exclusively based on ion sizes, becomes problematic in an attempt to explain the difference in T_S between STO and ETO. Neither does it explain the weaker octahedral distortion in $EuTi_{1-x}Nb_xO_3$ with increasing Nb concentration. It has been suggested that the high T_S of ETO compared to STO is associated with the hybridization between Eu f states and Ti d orbitals, which is also believed to be the origin of the giant spin-lattice coupling present in ETO [34]. Previous studies have shown that Nb doping enhances T_S of STO to higher temperatures due to the local changes in the hybridization between the (Ti, Nb)-d orbitals and O-2 p orbitals [35]. Another important factor is the covalency of the transition metal–oxygen bond [36,37]. *Ab initio* calculations have shown that the octahedral tilting angle in KMF_3 (M = transition metal) decreases linearly with the electron occupancy of the π-bonding t_{2g} orbitals of the transition metal. In the present system, Ti^{4+} has a $3d^0$ configuration. In contrast, Nb^{4+} possesses one electron in the t_{2g} orbitals, which most likely alters the covalency of the (Ti,Nb)-O bond and results in a weaker lattice distortion at low temperatures. It is noteworthy that $EuNbO_3$ is reported to remain cubic at room temperature, and octahedral tilting does not occur [38].

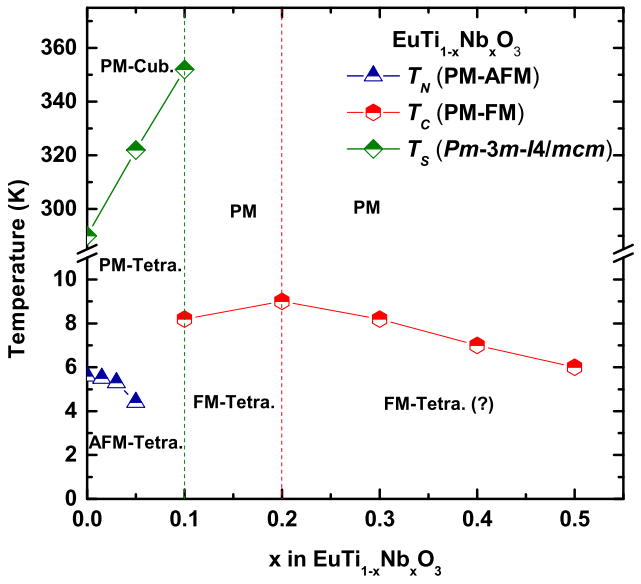

FIG. 8. (Color online) The temperature of the structural and magnetic phase transition vs Nb content x in $EuTi_{1-x}Nb_xO_3$.

V. SUMMARY

In conclusion, we have investigated the structural and magnetic transitions in both polycrystalline and single-crystal samples of $EuTi_{1-x}Nb_xO_3$ ($0 \leqslant x \leqslant 0.3$) using synchrotron powder XRD, resonant ultrasound spectroscopy, and magnetization measurements. The cubic ($Pm\bar{3}m$) to tetragonal ($I4/mcm$) structural phase transition in pure and doped $EuTiO_3$ is characterized by a steplike elastic softening in C_{44}, C_{11}, and $C' = \frac{1}{2}(C_{11} - C_{12})$. Nb substitution for Ti significantly enhances T_S to higher temperatures ($T_S = 322$ K and 353 K for $EuTi_{0.95}Nb_{0.05}O_3$ and $EuTi_{0.9}Nb_{0.1}O_3$, respectively). In contrast, the octahedral tilting angle decreases with increasing Nb doping, which is possibly caused by the introduction of t_{2g} electrons on the Ti site. In the meantime, the introduction of itinerant t_{2g} electrons switches the magnetic ground state of $EuTiO_3$ from AFM to FM. Our study emphasizes the important role of the covalency of the transition metal–oxygen bond in determining the octahedral tilting amplitude and magnetic ground state in the present system. Band structure calculations

of $EuTi_{1-x}Nb_xO_3$ will be useful to further examine how the hybridization between the Eu-f, (Ti,Nb)-d, and O-p orbitals changes with electron doping concentration on the transition metal site.

ACKNOWLEDGMENTS

L.L. acknowledges useful discussions with Dr. A. Bussmann-Holder. This research (L.L. and D.G.M.) is funded in part by the Gordon and Betty Moore Foundation's EPiQS Initiative through Grant No. GBMF4416. J.R.M. and J.-Q.Y. acknowledge support from the U.S. Department of Energy, Basic Energy Sciences, Materials Sciences and Engineering Division. Z.L.D. and H.D.Z. are supported by NSF-DMR-1350002. Use of the Advanced Photon Source at Argonne National Laboratory was supported by the U.S. Department of Energy, Office of Science, Office of Basic Energy Sciences, under Contract No. DE-AC02-06CH11357.

[1] M. Imada, A. Fujimori, and Y. Tokura, Rev. Mod. Phys. **70**, 1039 (1998).
[2] P. A. Fleury, J. F. Scott, and J. M. Worlock, Phys. Rev. Lett. **21**, 16 (1968).
[3] G. Shirane and Y. Yamada, Phys. Rev. **177**, 858 (1969).
[4] A. D. Bruce, K. A. Müller, and W. Berlinger, Phys. Rev. Lett. **42**, 185 (1979).
[5] A. Bussmann-Holder, H. Büttner, and A. R. Bishop, Phys. Rev. Lett. **99**, 167603 (2007).
[6] T. Katsufuji and H. Takagi, Phys. Rev. B **64**, 054415 (2001).
[7] D. S. Ellis, H. Uchiyama, S. Tsutsui, K. Sugimoto, K. Kato, D. Ishikawa, and A. Q. R. Baron, Phys. Rev. B **86**, 220301 (2012).
[8] A. Bussmann-Holder, J. Köhler, R. K. Kremer, and J. M. Law, Phys. Rev. B **83**, 212102 (2011).
[9] J. Koehler, R. Dinnebier, and A. Bussmann-Holder, Phase Transitions **85**, 949 (2012).
[10] M. Allieta, M. Scavini, L. J. Spalek, V. Scagnoli, H. C. Walker, C. Panagopoulos, S. S. Saxena, T. Katsufuji, and C. Mazzoli, Phys. Rev. B **85**, 184107 (2012).
[11] V. Goian, S. Kamba, O. Pacherová, J. Drahokoupil, L. Palatinus, M. Dušek, J. Rohlíček, M. Savinov, F. Laufek, W. Schranz *et al.*, Phys. Rev. B **86**, 054112 (2012).
[12] Z. Guguchia, H. Keller, J. Köhler, and A. Bussmann-Holder, J. Phys.: Condens. Matter **24**, 492201 (2012).
[13] J.-W. Kim, P. Thompson, S. Brown, P. S. Normile, J. A. Schlueter, A. Shkabko, A. Weidenkaff, and P. J. Ryan, Phys. Rev. Lett. **110**, 027201 (2013).
[14] D. S. Ellis, H. Uchiyama, S. Tsutsui, K. Sugimoto, K. Kato, and A. Q. Baron, Phys. B (Amsterdam, Neth.) **442**, 34 (2014).
[15] D. Bessas, K. Z. Rushchanskii, M. Kachlik, S. Disch, O. Gourdon, J. Bednarcik, K. Maca, I. Sergueev, S. Kamba, M. Ležaić *et al.*, Phys. Rev. B **88**, 144308 (2013).
[16] K. Z. Rushchanskii, N. A. Spaldin, and M. Ležaić, Phys. Rev. B **85**, 104109 (2012).
[17] Y. Yang, W. Ren, D. Wang, and L. Bellaiche, Phys. Rev. Lett. **109**, 267602 (2012).
[18] T. Birol and C. J. Fennie, Phys. Rev. B **88**, 094103 (2013).
[19] B. J. Kennedy, G. Murphy, E. Reynolds, M. Avdeev, H. E. R. Brand, and T. Kolodiazhnyi, J. Phys.: Condens. Matter **26**, 495901 (2014).
[20] L. J. Spalek, S. S. Saxena, C. Panagopoulos, T. Katsufuji, J. A. Schiemer, and M. A. Carpenter, Phys. Rev. B **90**, 054119 (2014).
[21] J. H. Lee, L. Fang, E. Vlahos, X. Ke, Y. W. Jung, L. F. Kourkoutis, J.-W. Kim, P. J. Ryan, T. Heeg, M. Roeckerath *et al.*, Nature (London) **466**, 954 (2010).
[22] L. Li, H. Zhou, J. Yan, D. Mandrus, and V. Keppens, APL Mater. **2**, 110701 (2014).
[23] A. Migliori, J. Sarrao, W. M. Visscher, T. Bell, M. Lei, Z. Fisk, and R. Leisure, Phys. B (Amsterdam, Neth.) **183**, 1 (1993).
[24] B. H. Toby, J. Appl. Crystallogr. **34**, 210 (2001).
[25] T. Katsufuji and Y. Tokura, Phys. Rev. B **60**, R15021 (1999).
[26] R. O. Bell and G. Rupprecht, Phys. Rev. **129**, 90 (1963).
[27] Y. P. Varshni, Phys. Rev. B **2**, 3952 (1970).
[28] W. Rehwald, Adv. Phys. **22**, 721 (1973).
[29] J. C. Slonczewski and H. Thomas, Phys. Rev. B **1**, 3599 (1970).
[30] K. Roleder, A. Bussmann-Holder, M. Górny, K. Szot, and A. Glazer, Phase Transitions **85**, 939 (2012).
[31] J. L. Bettis, M.-H. Whangbo, J. Köhler, A. Bussmann-Holder, and A. R. Bishop, Phys. Rev. B **84**, 184114 (2011).
[32] A. Bussmann-Holder, J. Kohler, and M.-H. Whangbo, Z. Anorg. Allg. Chem. **641**, 180 (2015).
[33] R. D. Shannon, Acta Crystallogr., Sect. A **32**, 751 (1976).
[34] H. Akamatsu, Y. Kumagai, F. Oba, K. Fujita, K. Tanaka, and I. Tanaka, Adv. Funct. Mater. **23**, 1864 (2013).
[35] D. Bäuerle and W. Rehwald, Solid State Commun. **27**, 1343 (1978).
[36] P. Garcia-Fernandez, J. A. Aramburu, M. T. Barriuso, and M. Moreno, J. Phys. Chem. Lett. **1**, 647 (2010).
[37] A. Cammarata and J. M. Rondinelli, J. Chem. Phys. **141**, 114704 (2014).
[38] A. Simon and G. Svensson, J. Alloys Compd. **226**, 24 (1995).